

## RESEARCH ARTICLE



# Spectral Limit of the Optical Behavior Between Film and Substrate for a Fluorine-Doped Tin Oxide (FTO) Transparent Conductive Layer

David Barrios-Puerto<sup>1,\*</sup><sup>1</sup>Universidad Carlos III de Madrid, Spain

**Abstract:** The optical constants of a fluorine-doped tin oxide (FTO) transparent conductive layer (of 400 nm thickness), deposited over a glass (*G*) substrate, were determined from the collimated transmittance (*T*) and reflectance (*R*) optical measurements of a bilayer FTOG sample in the solar wavelength range (from 250 nm to 2500 nm). The three-extinction matching requirement (3eMR) phenomenon was used as a feedback system to validate the accuracy of the optical constants results, obtained by fitting to the collimated *T* and *R* solutions of the four-flux model (4FM). The same extinction coefficients ( $\epsilon$ ) were observed than the obtained when computing light fluxes at the interfaces and substituting into the 4FM collimated differential equations (CDE). The compression of the wavelength of the incident light inside *G* and FTO layers was validated by computing  $\epsilon$  from optical constants. Despite a layer is considered a thin film when its thickness is lower than the wavelength of incident light beam, and a substrate when higher, the 3eMR allowed to determine the spectral limit of the FTO layer behavior, as a substrate and as a film, at 1200 nm (instead of at 400 nm, i.e., three times higher). FTO layer behaves as a substrate, for the shorter wavelength range of the solar spectrum (SWRSS), and as a film, for the longer wavelength range of the solar spectrum (LWRSS). The thickness gradients of the forward and backward (for&back) collimated light fluxes were determined at the glass substrate of the *G* and FTOG samples and for the SWRSS of the FTO as a substrate layer. Then, for the LWRSS, the thickness gradients for the complex magnitude and phase (Bode plots) of for&back electric fields of the FTO film layer have been spectrally determined and represented by means of imaginary versus real parts (Nyquist plots) depending on wavelength.

**Keywords:** optical constants, extinction coefficients, transparent conductors, thin film layers, complex electric fields

## 1. Introduction

Transparent conductive (TC) materials are of interest in solar cells, for collecting electrical current in photovoltaic applications, and in electrochromic (EC) smart windows, where electrical charge is inserted or extracted, required to change their optical appearance [1]. One option for these materials is fluorine-doped tin oxide (FTO = SnO<sub>2</sub>:F), used for thin films. FTO can be deposited over ultrasonic or pneumatic spray pyrolysis, showing higher transmittance (*T*) in the first case [2]. The size of crystals decreases with concentration in FTO co-doped with Erbium when prepared via nebulizer spray pyrolysis for optoelectronic applications [3]. Besides FTO, Indium-doped tin oxide (ITO = SnO<sub>2</sub>:In) is also widely used as a TC material in thin films nowadays. When ITO is deposited over PET substrate, extinction of light by scattering is higher than by absorption, resulting in a high albedo [4]. In other cases, such as for antireflection coatings, an increased scattering is directly related to an increment in the efficiency of thin film photo-electronic devices [5]. Flat antireflection coatings showing lower reflectance (*R*) of the substrate were studied in a system of layers for coherent (for thin layers) and incoherent (for thick layers) light [6]. The coherency of light depends on the multiple interferences between incident and

reflected waves at the different interfaces, losing the phase information which results in a loss in coherence. This loss can be caused also by the thickness of the coatings that increases the coherence length of the incident light [7, 8]. It is interesting to determine the optical refractive index for manufacturing multilayer mirrors with desired spectral characteristics [9]. In other cases, the refractive index can show different profiles of inhomogeneous thin films when deposited onto non-absorbing substrates [10]. Optical constants of thin films can be determined by ellipsometry [11], by the transfer matrix [12, 13], and by the scattering matrix [12, 14], or used to simulate *T* and *R* by means of Fresnel transmission ( $\tau$ ) and reflection ( $\rho$ ) coefficients for both polarizations of light [15].

In this work, the optical constants of a FTO layer of 400 nm thickness are determined in the wavelength range of the solar spectrum (WRSS) by using a bilayer FTOG sample (FTO deposited over a glass substrate) and the methods described in Born and Wolf, Knittel, Harbecke and Pfrommer et al. [16–19] for thin films, based on Fresnel  $\tau$  and  $\rho$  coefficients. According to Pfrommer et al. [19], a thin layer has the thickness of the order of the wavelength of light or less. This would mean that the FTO would behave as a film for lower wavelength than 400 nm and as a substrate for higher wavelength than 400 nm, i.e., the expected spectral limit. However, in this work, this spectral limit seems to be three times higher, i.e., 1200 nm. A phenomenon called three-extinction matching requirement (3eMR), observed in previous

\*Corresponding author: David Barrios-Puerto, Universidad Carlos III de Madrid, Spain. Email: dbarrios@ing.uc3m.es and dbarriosp76@gmail.com

recent works [20–22], was here used to determine this spectral limit of the optical behavior as a film or as a substrate. This is because extinction ( $\epsilon$ ) coefficients only apply for substrate layers, but not for film layers. The 3eMR phenomenon is described in detail in the Sections 3.2 and 4.1, including equations and plots. Hence, the FTO behaves as a film for the longer WRSS (LWRSS) and as a substrate for the shorter WRSS (SWRSS). The same FTO layer of the FTOG sample can be used as a TC electrode deposited over glass ( $G$ ) for inorganic  $\text{WO}_3$  and NiO-based EC devices (ECD), i.e., a smart window technology [23]. Seven layers (glass/FTO/ $\text{WO}_3$ /electrolyte/NiO/FTO/glass) are included in the sandwich structure of these ECDs. Under a low DC voltage applied,  $\text{WO}_3$  layer switches from bleached-uncolored to bluish-colored optical state, and NiO layer switches from bleached-uncolored to brownish-colored optical state. Since the FTO and the electrolyte [20] are transparent layers, the whole ECD then switches from a bleached-uncolored optical state to a neutral gray-colored optical state. According to a recent characterization of four  $\text{WO}_3$ -NiO ECDs, with single and double thickness of 120 nm and 240 nm combinations (i.e.,  $1 \times 1$ ,  $1 \times 2$ ,  $2 \times 1$ , and  $2 \times 2$ ) of the active  $\text{WO}_3$  and NiO layers, a new procedure was used to force the 3eMR. This new procedure was also required for two other smart windows samples characterized in Barrios [22]: a suspended particle device (SPD), at dark-off and clear-on optical states, and a polymer-dispersed liquid crystal (PDLC), at translucent-off and transparent-on optical states. This new procedure was required since the three substrate layers sandwich structure (TSLSS) considered (i.e., G-X-G) was only approximated and not exact (unlike with the glass/electrolyte/glass (GEG) sample [20], where the exact sandwich structure was considered due to the similarity between the TSLSS and the constructed three layers). This means that, in Barrios [22], the TC thin film layers were neglected for the SPD (G-SPD-G) sample and for the PDLC (PET-PDLC-PET) sample (PET was used instead of  $G$  with the PDLC sample). For the four  $\text{WO}_3$ -NiO ECDs, the five layers (FTO/ $\text{WO}_3$ /electrolyte/NiO/FTO) inside of the ECDs were considered as a single layer (G-ECD-G). The optical constants and the spectral limit of the optical behavior of FTO obtained in this work are then thought to be used in future works, in order to determine separately  $\text{WO}_3$  and NiO optical constants, at bleached-off and colored-on optical states of the four ECDs. Hence, the results of the FTO here determined are of interest in order to improve the TSLSS mentioned recent study by considering seven layers, including substrate and thin films, instead of three substrates, at the sandwich structure of the ECDs. For that, the optical constants of the electrolyte were previously obtained from the GEG sample [20], when it was observed for the first time the 3eMR, i.e., the same  $\epsilon$  coefficients are observed when computed from the complex refractive index and when computed from the two forward and backward (for&back) collimated differential equations (CDE) of the four-flux model (4FM) [24–26]. Then, from the diffuse differential equations (DDE) of the 4FM, intrinsic scattering and absorption coefficients ( $\alpha$  and  $\beta$ , respectively, being  $\epsilon = \alpha + \beta$ ) were obtained, thanks to four intuitive relations used for approximating average crossing parameters (ACP) and forward scattering ratio (FSR) affecting diffuse light fluxes [20] (both ACP and FSR being differentiated for for&back light fluxes). Then, from the 4FM parameters, extrinsic scattering and absorption coefficients ( $S$  and  $K$ , respectively) were computed using the differential equations of the two-flux model (2FM) [27] for total light fluxes, i.e., the sum of collimated and diffuse light fluxes [28]. Decoupling  $\alpha$  and  $\beta$  from  $\epsilon$  was carried out using the CDE and DDE-based inverse method [20, 22], i.e., using only the  $T$  and  $R$  measurements

and not considering any other parameter such as size, shape, or concentration of the small particles. This inverse method was referred as the hard problem, in [29], while the direct method was referred as the easy problem.

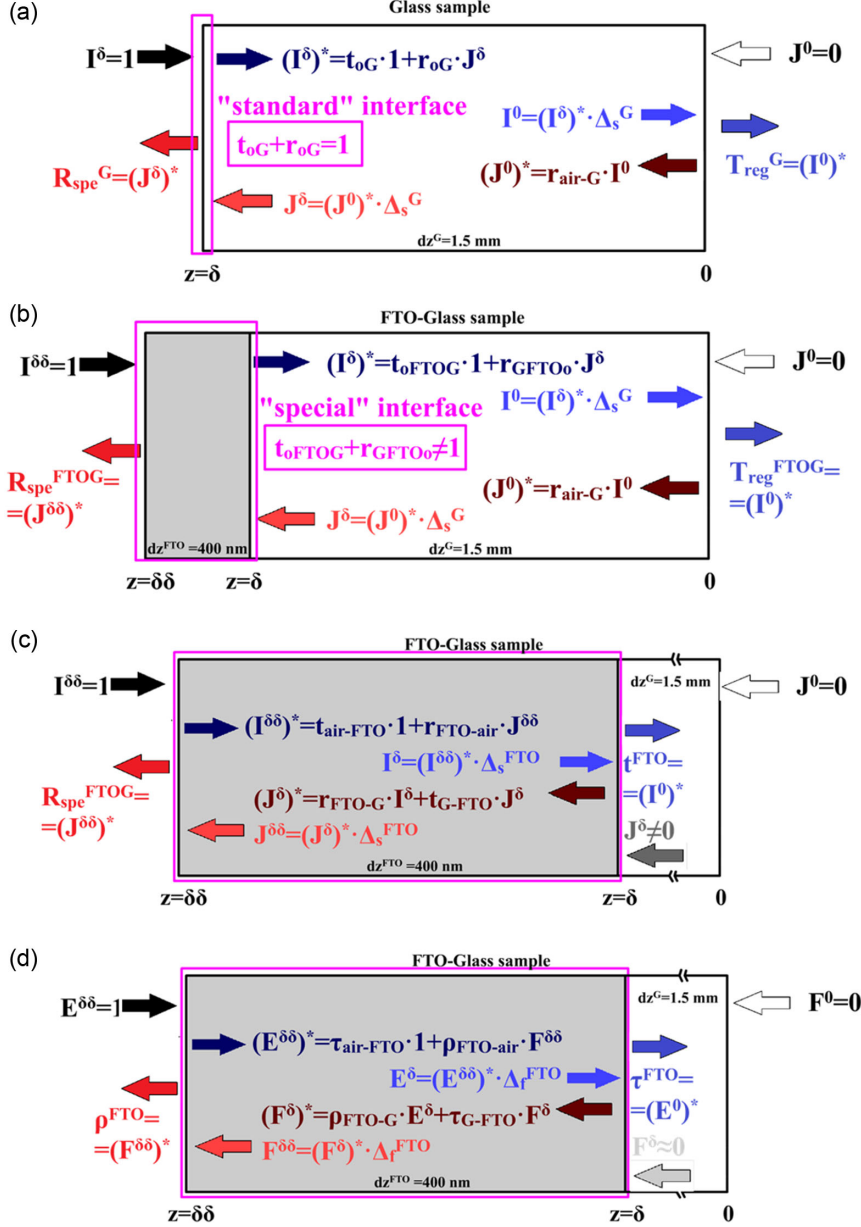
As recently carried out with an ITO layer (film of 26 nm thick) [21] deposited on a glass substrate in an ITOG sample, the thickness gradients plots (TGP) of light fluxes (LF), for forward (I) and backward (J) and the TGP of complex electric fields (CEF), for forward (E) and backward (F), were here determined for the FTOG sample. Note that the wavelength ( $\lambda$ ) compression of light inside of a material with refractive index  $n$  ( $\lambda_n = \lambda/n$ ) was required in  $G$ , GEG, ITOG, and FTOG samples, for observing the 3eMR. Note also that  $\epsilon$  is computed from the optical constants, i.e.,  $\epsilon^{\text{km}} = 4\pi\kappa/\lambda_n = 4\pi\kappa n/\lambda$ , but it can also be determined from the LFs at the extremes of the substrate layer using the 4FM-CDE (forward  $\epsilon^i$  and backward  $\epsilon^j$ ). The 3eMR phenomenon means that  $\epsilon^{\text{km}} = \epsilon^i = \epsilon^j$ . Using the FTO optical constants determined in this work with the FTOG sample, LF-TGP and CEF-TGP were obtained. LF-TGP were determined at the substrate  $G$  layer and at the FTO layer for the SWRSS (from 250 nm to 1200 nm), where the FTO behaves as a substrate, with the bilayer (substrate-substrate) sandwich structure. CEF-TGP were determined at the FTO layer for the LWRSS (from 1200 nm to 2500 nm), where the FTO behaves as a film, with the bilayer (film-substrate) sandwich structure. Magnitude and phase (Bode) and imaginary versus real parts (Nyquist) wavelength-dependent diagrams (WDD) were also determined for both for&back CEF (in the same way than with the ITOG sample as in Barrios [21]), for six different positions inside the FTO layer, i.e., at  $z = 0$ , 80, 160, 240, 320 and 400 nm. The 3eMR phenomenon leads to obtain the TGP not only in this work, for the FTOG bilayer sample, but also for the ITOG bilayer (film-substrate) sample [21], for the electrolyte inner layer of the TSLSS GEG sample [20], and for the approximated TSLSS ECD, SPD, and PDLC samples [22]. In any case, the optical constants and spectral limit of the optical behavior of the FTO layer between film and substrate here determined would be of interest for future works with  $\text{WO}_3$ -NiO-based ECDs.

## 2. Samples of the Experiment

Collimated  $T$  and  $R$  of  $G$  and FTOG samples were measured using the spectrometer Perkin Elmer Lambda 950 in the WRSS (250-2500 nm), with a 5 nm steps. Figure 1(a) and (b) shows the sandwich structures of  $G$  and FTOG samples, respectively. LF at the inner of the  $G$  substrate layers are computed from regular  $T$  ( $T_{\text{reg}}$ ) and specular  $R$  ( $R_{\text{spe}}$ ) measurements, exiting the sample through the top and bottom interfaces, at  $z = \delta$  and  $z = 0$ , respectively, for the  $G$  sample in Figure 1(a), and at  $z = \delta\delta$  and  $z = 0$ , respectively, for the FTOG sample in Figure 1(b). Figure 1(c) shows the LF inside of the FTO layer considered as a substrate, for the SWRSS. Here, collimated interface  $T$  and  $R$  ( $t$  and  $r$ ) are determined for the top interface, at  $z = \delta\delta$ , between outside air and FTO, and for the middle interface, at  $z = \delta$ , between FTO and glass. Figure 1(d) shows the CEF of light inside of the FTO layer considered as a film, for the LWRSS. Here, the Fresnel  $\tau$  and  $\rho$  coefficients are determined for top interface, at  $z = \delta\delta$ , and for the middle interface, and at  $z = \delta$ . The bottom interfaces of both  $G$  and FTOG samples are standard (i.e., between two substrates or thick layers, such as  $G$  and outer air). The top interface of the  $G$  sample is also standard (between outer air and  $G$ ). The FTO layer behaves as a substrate in Figure 1(c) (for  $\lambda < 1200$  nm) and as a film in Figure 1(d) (for  $\lambda \geq 1200$  nm). For the LWRSS, the FTO layer of the FTOG sample behaves as a top special interface showing absorption (i.e., the result of adding interface  $T$  and  $R$  is lower than unity), being the sandwich

Figure 1

Sandwich structures with LF (forward I and backward J), at the G substrate layer of the (a) G and (b) FTOG samples, and (c) at the FTO layer considered as a substrate, and (d) with CEF (forward E and backward F) at the FTO layer considered as a film.  $\epsilon$  attenuation factor of a G layer  $\Delta_s^G$ , in (a) and (b), and  $\epsilon$  attenuation factor of FTO layer considered as a substrate  $\Delta_s^{FTO}$ , for the SWRSS with  $\lambda < 1200$  nm, in (c), and attenuation factor of FTO layer considered as a film  $\Delta_f^{FTO}$ , for the LWRSS with  $\lambda \geq 1200$  nm, in (d)



structure (film-substrate) of Figure 1(d) the same than for the ITOG sample [21]. The asterisk (\*) of the arrows in Figure 1 means that these arrows do not end at the interfaces, but start (being computed as the sum of  $T$  and  $R$  arrows ending at the interfaces, as explained in Barrios [21]). These asterisk arrows are explained in detail in the following sections.

### 3. Theoretical Aspects

This part consists of two subparts: first, the complex refractive index methodology used for film and substrate layers, and second, the 4FM CDE and the 3eMR.

#### 3.1. Complex refractive index of glass substrate and of FTO behaving as a substrate and as a film

Interface and layer matrixes are involved in the following explanation. From the complex refractive index in Equation (1), it is computed the Fresnel  $\tau$  and  $\rho$  coefficients for both polarizations of light in Equations (2)–(5), required to determine collimated interface  $T$  and  $R$  ( $t$  and  $r$ ) in Equations (6) and (7), respectively. Interface matrix  $M_{oi}^1$  of Equation (8), from outside "o" (air) to inside "i" (air) mediums, uses the averaged values of  $S$  and  $P$  polarizations. Light fluxes  $I$  and  $J$  are actually helicoidal electromagnetic light beams of spectral irradiance in  $mW/m^2$  but

here considered without units and normalized to unity of input illumination through the top interface. Extinction attenuation factor  $\Delta_s(d) = e^{-\text{exn} \cdot dz}$ , implicit in Equation (9), is used to determine the substrate layer matrix  $N_s^I$  of Equation (10). Equation (11) shows the matrix substrate multiplication of the  $G$  sample consisting of a single substrate layer. Equation (12) is the result of illuminating only through the top interface (by doing  $I_o = 1$  and  $J_i = 0$  and considering  $J_o = R_{cc}^G$  and  $I_i = T_{cc}^G$ , i.e., fitting to the collimated measurements  $T_{reg}^G$  and  $R_{spe}^G$  to find  $n^G$  and  $\kappa^G$ ). Equation (13) shows the matrix substrate multiplication of a FTOG bilayer sample. The only difference with the  $G$  sample is the  $M_{\text{OFTOG}}^I$  interface matrix, instead of the  $M_{oG}^I$  interface matrix of the  $G$  sample (by doing  $I_o = 1$  and  $J_i = 0$  and considering  $J_o = R_{cc}^{\text{FTOG}}$  and  $I_i = T_{cc}^{\text{FTOG}}$ , i.e., fitting to the collimated measurements  $T_{reg}^{\text{FTOG}}$  and  $R_{spe}^{\text{FTOG}}$  to find  $n^{\text{FTO}}$  and  $\kappa^{\text{FTO}}$ ). The  $M_{\text{OFTOG}}^I$  interface matrix is determined from Equations (14)–(32), for both WRSS, i.e., SWRSS (shorter) and LWRSS (longer). Equation (14) is to CEF at film layers as Equation (8) is to LF at substrate layers. Attenuation factor  $\Delta_f(d)$  of a layer considered as a film is determined using Equation (15). The wavelength involved is related to the film layer ( $\lambda^{\text{FTO}} = \lambda/n^{\text{FTO}}$ ), for the LWRSS, when the thickness of the FTO layer is lower than one-third of the wavelength of incident light fluxes (i.e., 1200 nm/3 = 400 nm). Film layer matrix  $N_f^E$  is shown in Equation (16). Matrix film  $M_{\text{OFTOG}}^E$  after multiplying interface and layer for CEF appears in Equation (17) between outside air and  $G$ . Equation (18) is the result of illuminating only through the top outer interface (by doing  $E_o = 1$  and  $F_G = 0$  and considering  $F_o = \rho_{\text{oFTOG}}$  and  $E_G = \tau_{\text{oFTOG}}$ ). Equation (19) is the result of illuminating only through the middle interface (by doing  $E_o = 0$  and  $F_G = 1$  and considering  $F_o = \rho_{\text{GFTOo}}$  and  $E_G = \tau_{\text{GFTOo}}$ ).

$$n' = n - i\kappa \quad (1)$$

$$\tau_{oi}^S = \frac{2n'_o}{n'_o + n'_i} \quad (2)$$

$$\rho_{oi}^S = \frac{n'_o - n'_i}{n'_o + n'_i} \quad (3)$$

$$\tau_{oi}^P = \frac{2n'_o}{n'_o + n'_i} \quad (4)$$

$$\rho_{oi}^P = \frac{n'_i - n'_o}{n'_o + n'_i} \quad (5)$$

$$t_{oi}^X = \text{Re}\left(\frac{n'_i}{n'_o}\right) \cdot |\tau_{oi}^X|^2 = \text{Re}\left(\frac{n'_i}{n'_o}\right) \cdot \tau_{oi}^X \cdot \text{conj}(\tau_{oi}^X) \quad (6)$$

$$r_{oi}^X = |\tau_{oi}^X|^2 = \rho_{oi}^X \cdot \text{conj}(\rho_{oi}^X) \quad (7)$$

$$\begin{bmatrix} I_o \\ J_o \end{bmatrix} = \begin{bmatrix} \frac{1}{t_{oi}} & \frac{-r_{oi}}{t_{oi}} \\ \frac{r_{oi}}{t_{oi}} & t_{oi} - \frac{r_{oi}}{t_{oi}} \end{bmatrix} \cdot \begin{bmatrix} I_i \\ J_i \end{bmatrix} = M_{oi}^I \cdot \begin{bmatrix} I_i \\ J_i \end{bmatrix} \quad (8)$$

$$\Delta_s(d) = \frac{I_2}{I_1} = \exp\left(-\frac{4\pi\kappa}{\lambda_n} d\right) = \exp\left(-\frac{4\pi\kappa n}{\lambda} d\right) \quad (9)$$

$$\begin{bmatrix} I_s(1) \\ J_s(1) \end{bmatrix} = \begin{bmatrix} \frac{1}{\Delta_s(d)} & 0 \\ 0 & \Delta_s(d) \end{bmatrix} \cdot \begin{bmatrix} I_s(2) \\ J_s(2) \end{bmatrix} = N_s^I \cdot \begin{bmatrix} I_s(2) \\ J_s(2) \end{bmatrix} \quad (10)$$

$$\begin{bmatrix} I_o \\ J_o \end{bmatrix} = M_{oG}^I \cdot N_G^I \cdot M_{Gi}^I \cdot \begin{bmatrix} I_i \\ J_i \end{bmatrix} \quad (11)$$

$$\begin{bmatrix} 1 \\ R_c^G \end{bmatrix} = M_{oG}^I \cdot N_G^I \cdot M_{Gi}^I \cdot \begin{bmatrix} T_{cc}^G \\ 0 \end{bmatrix} \quad (12)$$

$$\begin{bmatrix} 1 \\ R_{cc}^{\text{FTOG}} \end{bmatrix} = M_{\text{oFTOG}}^I \cdot N_G^I \cdot M_{Gi}^I \cdot \begin{bmatrix} T_{cc}^{\text{FTOG}} \\ 0 \end{bmatrix} \quad (13)$$

$$\begin{bmatrix} E_o \\ F_o \end{bmatrix} = \begin{bmatrix} \frac{1}{\tau_{oi}} & \frac{\rho_{oi}}{t_{oi}} \\ \frac{\rho_{oi}}{\tau_{oi}} & \frac{1}{\tau_{oi}} \end{bmatrix} \cdot \begin{bmatrix} E_i \\ F_i \end{bmatrix} = M_{oi}^E \cdot \begin{bmatrix} E_i \\ F_i \end{bmatrix} \quad (14)$$

$$\Delta_f(d) = \frac{E_2}{E_1} = \exp\left(-i\frac{2\pi n}{\lambda_{\text{FTO}}} d\right) \cdot \exp\left(-\frac{2\pi\kappa}{\lambda_{\text{FTO}}} d\right) \quad (15)$$

$$\begin{bmatrix} E_f(1) \\ F_f(1) \end{bmatrix} = \begin{bmatrix} \frac{1}{\Delta_f(d)} & 0 \\ 0 & \Delta_f(d) \end{bmatrix} \cdot \begin{bmatrix} E_f(2) \\ F_f(2) \end{bmatrix} = N_f^E \cdot \begin{bmatrix} E_f(2) \\ F_f(2) \end{bmatrix} \quad (16)$$

$$\begin{bmatrix} E_o \\ F_o \end{bmatrix} = M_{\text{oFTOG}}^E \cdot N_{\text{FTO}}^E \cdot M_{\text{FTOG}}^E \cdot \begin{bmatrix} E_G \\ F_G \end{bmatrix} = M_{\text{oFTOG}}^E \cdot \begin{bmatrix} E_G \\ F_G \end{bmatrix} \quad (17)$$

$$\begin{aligned} \begin{bmatrix} 1 \\ \rho_{\text{oFTOG}} \end{bmatrix} &= M_{\text{oFTOG}}^E \cdot N_{\text{FTO}}^E \cdot M_{\text{FTOG}}^E \cdot \begin{bmatrix} \tau_{\text{oFTOG}} \\ 0 \end{bmatrix} \\ &= M_{\text{oFTOG}}^E \cdot \begin{bmatrix} \tau_{\text{oFTOG}} \\ 0 \end{bmatrix} \end{aligned} \quad (18)$$

$$\begin{aligned} \begin{bmatrix} 0 \\ \tau_{\text{GFTOo}} \end{bmatrix} &= M_{\text{oFTOG}}^E \cdot N_{\text{FTO}}^E \cdot M_{\text{FTOG}}^E \cdot \begin{bmatrix} \rho_{\text{GFTOo}} \\ 1 \end{bmatrix} \\ &= M_{\text{oFTOG}}^E \cdot \begin{bmatrix} \rho_{\text{GFTOo}} \\ 0 \end{bmatrix} \end{aligned} \quad (19)$$

According to [18, 19] and doing  $M = M_{\text{OFTOG}}^E = M_{\text{oFTOG}}^E \cdot N_{\text{FTO}}^E \cdot M_{\text{FTOG}}^E$ , the expressions for determining  $\tau$  &  $\rho$  in both light senses of the FTO film are  $\tau_{\text{oFTOG}} = 1/M_{11}$ ,  $\rho_{\text{oFTOG}} = M_{21}/M_{11}$ ,  $\tau_{\text{GFTOo}} = (M_{11} \cdot M_{22} - M_{12} \cdot M_{21})/M_{11}$ , and  $\rho_{\text{GFTOo}} = -M_{12}/M_{11}$ . Here, Equations (20)–(23) are the same as Equations (59) and (60) from page 62 of Born and Wolf [16], or the Equations 2.32a, b and 2.33a, b of Knittl [17]. From  $\tau$  &  $\rho$ , the  $T$  and  $R$  of the FTO film considered as a special interface ( $t$  and  $r$ ) in forward & back light senses are determined by means of Equations (24)–(27), as it is done for standard interfaces in Equations (6) and (7). Hence,  $r_{\text{oFTOG}}$ ,  $t_{\text{oFTOG}}$ ,  $r_{\text{GFTOo}}$ , and  $t_{\text{GFTOo}}$ , i.e., the collimated interface  $T$  and  $R$  of the FTO layer, are computed in two different ways: For the LWRSS,  $r_{\text{oFTOG}}$ ,  $t_{\text{oFTOG}}$ ,  $r_{\text{GFTOo}}$ , and  $t_{\text{GFTOo}}$ , i.e., the interface  $T$  and  $R$  of the FTO, as a film layer, are computed with Equations (24)–(27). For the SWRSS,  $r_{\text{oFTOG}}$ ,  $t_{\text{oFTOG}}$ ,  $r_{\text{GFTOo}}$ , and  $t_{\text{GFTOo}}$ , i.e., the interface  $T$  and  $R$  of the FTO, as a substrate layer, are computed with Equations (28)–(31). Note that the expected continuity of  $r_{\text{oFTOG}}$ ,  $t_{\text{oFTOG}}$ ,  $r_{\text{GFTOo}}$ , and  $t_{\text{GFTOo}}$  at the spectral limit of the optical behavior as a film and as substrate, at 1200 nm, is observed in the results of the next section. Then, using the same structure of the interface matrix  $M_{oi}^I$  of Equation (8) with  $r_{oi}$ ,  $t_{oi}$ ,  $r_{io}$ , and  $t_{io}$ ,  $M_{\text{OFTOG}}^I$  is determined in Equation (32) by means of  $r_{\text{oFTOG}}$ ,  $t_{\text{oFTOG}}$ ,  $r_{\text{GFTOo}}$ , and  $t_{\text{GFTOo}}$ . The matrix  $M_{\text{OFTOG}}^I$  uses collimated interface  $T$  and  $R$  when light fluxes cross FTO layer in both cases, i.e., in forward (oFTOG) light sense, from outside air to  $G$ , and in backward (GFTOo) light sense, from  $G$  to outside air.

$$\tau_{oFTOG} = \frac{1}{T_{11}} = \frac{\tau_{oG} \cdot \tau_{GFTO} \cdot \Delta_f(d)}{1 - \rho_{FTOo} \cdot \rho_{FTOG} \cdot \Delta_f(d)^2} \quad (20)$$

$$\rho_{oFTOG} = \frac{T_{21}}{T_{11}} = \frac{\rho_{oFTO} + \rho_{FTOG} \cdot \Delta_f(d)^2}{1 - \rho_{FTOo} \cdot \rho_{FTOG} \cdot \Delta_f(d)^2} \quad (21)$$

$$\tau_{GFTOo} = \frac{T_{11}T_{22} - T_{12}T_{21}}{T_{11}} = \frac{\tau_{GFTO} \cdot \tau_{FTOo} \cdot \Delta_f(d)}{1 - \rho_{FTOo} \cdot \rho_{FTOG} \cdot \Delta_f(d)^2} \quad (22)$$

$$\rho_{GFTOo} = \frac{-T_{12}}{T_{11}} = \frac{\rho_{GFTO} + \rho_{FTOo} \cdot \Delta_f(d)^2}{1 - \rho_{FTOo} \cdot \rho_{FTOG} \cdot \Delta_f(d)^2} \quad (23)$$

$$r_{oFTOG} = \rho_{oFTOG} \cdot \text{conj}(\rho_{oFTOG}) \quad (24)$$

$$t_{oFTOG} = \text{Real}\left(\frac{n_G - i \cdot \kappa_G}{n_{air}}\right) \cdot \tau_{oFTOG} \cdot \text{conj}(\tau_{oFTOG}) \quad (25)$$

$$r_{GFTOo} = \rho_{GFTOo} \cdot \text{conj}(\rho_{GFTOo}) \quad (26)$$

$$t_{GFTOo} = \text{Real}\left(\frac{n_{air}}{n_G - i \cdot \kappa_G}\right) \cdot \tau_{GFTOo} \cdot \text{conj}(\tau_{GFTOo}) \quad (27)$$

$$r_{oFTOG} = r_{FTO} + \frac{t_{FTO} \cdot t_{FTO} \cdot r_{FTOG} \cdot \Delta_s(d)^2}{1 - r_{FTO} \cdot r_{FTOG} \cdot \Delta_s(d)^2} \quad (28)$$

$$t_{oFTOG} = \frac{t_G \cdot t_{GFTO} \cdot \Delta_s(d)}{1 - r_{FTO} \cdot r_{FTOG} \cdot \Delta_s(d)^2} \quad (29)$$

$$r_{GFTOo} = r_{GFTO} + \frac{t_{GFTO} \cdot t_{FTOG} \cdot r_{FTO} \cdot \Delta_s(d)^2}{1 - r_{FTO} \cdot r_{FTOG} \cdot \Delta_s(d)^2} \quad (30)$$

$$t_{GFTOo} = \frac{t_{GFTO} \cdot \tau_{FTO} \cdot \Delta_s(d)}{1 - r_{FTO} \cdot r_{FTOG} \cdot \Delta_s(d)^2} \quad (31)$$

$$\begin{bmatrix} I_o \\ J_o \end{bmatrix} = \begin{bmatrix} \frac{1}{t_{oFTOG}} & \frac{-r_{GFTOo}}{t_{oFTOG}} \\ t_{GFTOo} & -\frac{r_{GFTOo} r_{oFTOG}}{t_{oFTOG}} \end{bmatrix} \cdot \begin{bmatrix} I_G \\ J_G \end{bmatrix} = M_{oFTOG}^I \cdot \begin{bmatrix} I_G \\ J_G \end{bmatrix} \quad (32)$$

Besides,  $r_{oFTOG}$ ,  $t_{oFTOG}$ ,  $r_{GFTOo}$ , and  $t_{GFTOo}$  are also required for computing the exact light fluxes at the  $G$  substrate layer, required for determining  $\varepsilon$  in the for&back light senses ( $\varepsilon_G^I$  and  $\varepsilon_G^J$ ) from the CDE of the 4FM [24–26]. In this way, since the 3 $\varepsilon$ MR was obtained at the  $G$  substrate layers of the two  $G$  and FTOG samples, LF-TGP could be plotted with accuracy for the  $G$  layers. Besides, due to the 3 $\varepsilon$ MR observed at the FTO layer considered as a substrate at the SWRSS, LF-TGP could also be plotted with accuracy for the FTO layer considered as a substrate. For that,  $r_{FTO}$ ,  $t_{FTO}$ ,  $r_{FTOG}$ ,  $t_{FTOG}$ ,  $r_G$ , and  $t_G$  must be computed in advance, using Equations (1)–(7), for outside air-FTO ( $r_{FTO}$  &  $t_{FTO}$ ), FTOG ( $r_{FTOG}$  &  $t_{FTOG}$ ), and  $G$ -inside air ( $r_G$  &  $t_G$ ) interfaces, respectively.

### 3.2. CDEs of 4FM and 3 $\varepsilon$ MR

4FM-CDE Equations (33) and (34) are symmetrical equations used for for&back light senses. From them, the forward  $\varepsilon_G^I$  and the backward  $\varepsilon_G^J$  were determined for the inner  $G$  substrate layer of the FTOG sample, by means of  $\Delta_G(d)$  observed in Figure 1(b). The 3 $\varepsilon$ MR of the  $G$  layer for the FTOG sample means that  $\varepsilon_G^I = \varepsilon_G^J = \varepsilon_G^{\text{kn}}$ . The 3 $\varepsilon$ MR of the  $G$  sample is not plotted in this work (since  $\varepsilon_G^I$  and  $\varepsilon_G^J$  are here related to the  $G$  layer of the FTOG sample, and not to the  $G$  layer of the  $G$  sample), but it can be found in Barrios [21]. Besides, 4FM-CDE Equations (35) and (36) are symmetrical equations used for determining the forward

$\varepsilon_{\text{FTO}}^I$  and the backward  $\varepsilon_{\text{FTO}}^J$  of the inner FTO considered as a substrate layer, at the SWRSS, in Figure 1(c).

$$\frac{dI}{dz} = \frac{(I^\delta)^* - (I^0)}{dz^G} = \varepsilon_G^I \cdot (I^\delta)^* \quad (33)$$

$$\frac{dJ}{dz} = \frac{(J^\delta) - (J^0)^*}{dz^G} = -\varepsilon_G^J \cdot J^\delta \quad (34)$$

$$\frac{dI}{dz} = \frac{(I^{\delta\delta})^* - (I^\delta)}{\text{FTO}} = \varepsilon_{\text{FTO}}^I \cdot (I^{\delta\delta})^* \quad (35)$$

$$\frac{dJ}{dz} = \frac{(J^{\delta\delta}) - (J^\delta)^*}{dz^{\text{FTO}}} = -\varepsilon_{\text{FTO}}^J \cdot J^{\delta\delta} \quad (36)$$

In Figure 1(a), the forward LF at the top interface of the  $G$  sample ( $I^\delta$ )\* is determined for air- $G$  standard interface. ( $I^\delta$ )\*, ( $J^0$ )\*  $I^0$ , and  $J^\delta$ , i.e., LF at the extremes of the  $G$  layer, were determined using  $T_{\text{reg}}^G$  and  $R_{\text{spe}}^G$  measurements, by means of Equations (37)–(40), and used in Equations (33) and (34) in order to determine  $\varepsilon_G^I$  and  $\varepsilon_G^J$ . The same values were computed for  $\varepsilon_G^I$  and  $\varepsilon_G^J$  than for  $\varepsilon_G^{\text{kn}}$ , due to the 3 $\varepsilon$ MR observed with the  $G$  sample using  $T_{\text{reg}}^G$  and  $R_{\text{spe}}^G$  measurements and with the ITOG sample using  $T_{\text{reg}}^{\text{ITOG}}$  and  $R_{\text{spe}}^{\text{ITOG}}$  measurements in Barrios [21]. The same procedure was carried out in this work for the FTOG sample with the  $G$  substrate layer of the FTOG sample. In Figure 1(b), the forward LF at the top interface of the FTOG sample ( $I^\delta$ )\* is determined for air-FTOG special interface. ( $I^\delta$ )\*, ( $J^0$ )\*  $I^0$  and  $J^\delta$ , i.e., LF at the extremes of the  $G$  layer were determined using  $T_{\text{reg}}^{\text{FTOG}}$  and  $R_{\text{spe}}^{\text{FTOG}}$  measurements, by means of Equations (41)–(44), and used in Equations (35) and (36) in order to determine  $\varepsilon_{\text{FTO}}^I$  and  $\varepsilon_{\text{FTO}}^J$ . The  $r_{oFTOG}$  parameter of Equation (42) was computed using Equation (24), for the LWRSS, and Equation (28), for the SWRSS. Besides, for the SWRSS, when the FTO is considered as a substrate layer, the LF-TGP inside of the FTO layer are obtained by computing the LFs at the extremes, in the 4FM-CDE Equations (35) and (36), i.e., ( $I^{\delta\delta}$ )\*,  $J^\delta$ ,  $J^{\delta\delta}$  and ( $J^\delta$ )\* of Figure 1(c), by means of Equations (45)–(48), respectively. Since the samples were only illuminated through the top interface, asterisked LFs are computed as the sum of transmitted and reflected components, for the top interface, in Equations (37), (41), and (45), being only the reflected component, for the bottom interface, since  $J^0 = 0$  (see Figure 1), in Equations (38), (42) and (46).

$$(I^\delta)_{\text{air-G}}^* = t_G \cdot 1 + r_G \cdot J^\delta \quad (37)$$

$$(J^0)_{\text{air-G}}^* = r_G \cdot I^0 \quad (38)$$

$$(I^0)_{\text{air-G}} = \frac{T_{\text{reg}}^G}{t_G} \quad (39)$$

$$(J^\delta)_{\text{air-G}} = \frac{R_{\text{spe}}^G - r_G}{t_G} \quad (40)$$

$$(I^\delta)_{\text{air-FTO-G}}^* = t_{oFTOG} \cdot 1 + r_{GFTOo} \cdot J^\delta \quad (41)$$

$$(J^0)_{\text{air-FTO-G}}^* = r_{oFTOG} \cdot I^0 \quad (42)$$

$$(I^0)_{\text{air-FTO-G}} = \frac{T_{\text{reg}}^{\text{FTOG}}}{t_G} \quad (43)$$

$$(J^\delta)_{\text{air-FTO-G}} = \frac{R_{\text{spe}}^{\text{FTOG}} - r_{oFTOG}}{t_{GFTOo}} \quad (44)$$

$$(I^{\delta\delta})_{air-FTO}^* = t_{FTO} \cdot 1 + r_{GFTO} \cdot J^{\delta\delta} \quad (45)$$

$$(J^{\delta})_{G-FTO}^* = r_{GFTO} \cdot I^{\delta} \quad (46)$$

$$(I^{\delta})_{FTO-G} = (I^{\delta})_{air-FTO-G}^* \cdot \Delta_S^I \quad (47)$$

$$(J^{\delta\delta})_{FTO-air} = \frac{R_{spe}^{FTOG} - r_{FTO}}{t_{FTO}} \quad (48)$$

The same for&back extinction coefficients  $\varepsilon_G^I$  and  $\varepsilon_G^J$  were computed using the Equations (33), (34), and (41)–(44) for the FTOG sample (or using the Equations (37)–(40) for the  $G$  sample, obtained in Barrios [21]), achieving the same value as  $\varepsilon_{kn}^G$ , in Equation (49). The attenuation of the LF at the  $G$  substrate is observed in Equation (9) since  $\Delta_S^G(d) = \exp(-\varepsilon_{kn}^G \cdot dz^G)$ . The same for&back  $\varepsilon_{FTO}^I$  and  $\varepsilon_{FTO}^J$ , determined by means of Equations (35), (36) and (45)–(48) for the FTO layer considered as a substrate, at the SWRSS, achieving the same value than  $\varepsilon_{FTO}^{kn}$ , in Equation (50). The attenuation of the LF at the FTO as a substrate is also observed in Equation (9) since  $\Delta_S^{FTO}(d) = \exp(-\varepsilon_{FTO}^{kn} \cdot dz^{FTO})$ . Then, Equations (51) and (52) are derived from Equation (15) for the real and imaginary parts (Re&Im-P) of the film attenuation required with CEF and computed at four intermediate positions inside the FTO considered as a film, i.e., between  $dz^0 = 0$  nm and  $dz^5 = 400$  nm with 80 nm steps, in order to obtain the CEF-TGP.

$$\varepsilon_G^{kn} = \frac{4\pi\kappa^G}{\lambda_n^G} = \frac{4\pi\kappa^G n^G}{\lambda} \quad (49)$$

$$\varepsilon_{FTO}^{kn} = \frac{4\pi\kappa^{FTO}}{\lambda_n^{FTO}} = \frac{4\pi\kappa^{FTO} n^{FTO}}{\lambda} \quad (50)$$

$$Real[\Delta_f(d)] = Real\left(\frac{E_2}{E_1}\right) = \exp\left(-\frac{2\pi\kappa^{FTO}}{\lambda_n^{FTO}} d\right) \cdot \cos\left(\frac{2\pi n^{FTO}}{\lambda_n^{FTO}} d\right) \quad (51)$$

$$Imag[\Delta_f(d)] = Imag\left(\frac{E_2}{E_1}\right) = \exp\left(-\frac{2\pi\kappa^{FTO}}{\lambda_n^{FTO}} d\right) \cdot \sin\left(\frac{2\pi n^{FTO}}{\lambda_n^{FTO}} d\right) \quad (52)$$

## 4. Results and Discussion

This part consists of three subparts: First, the LF and CEF determined at the interfaces. Second, the LF-TGP at  $G$  substrate layers of  $G$  and FTOG samples and the LF-TGP at the FTO layer considered as a substrate, in the SWRSS. Third, the CEF-TGP (Bode WDD) at the FTO layer considered as a film, in the LWRSS. Also in the third section, Nyquist WDD of the CEF are plotted, for both for&back light senses.

### 4.1. Light fluxes and complex electric fields determined at the interfaces

This section consists of two sets of eight plots: First, for LF (Figure 2), and then, for CEF (Figure 3). Perfect fittings are observed between measured and computed  $T$  and  $R$  for  $G$  and FTOG samples, in Figure 2(a) and (b) respectively. Re&Im-P of the complex refractive index, obtained for the  $G$  substrate layer and for the FTO layer considered as substrate and as a film, is shown in Figure 2(c) and (d), respectively. When  $n^{FTO} > n^G$  (in all the WRSS except the range from 1100 nm to 1520 nm), light travels at slower speed in the FTO layer than in the  $G$  layer. Note that  $\kappa^{FTO} \gg \kappa^G$  in Figure 2(d). Figure 2(e) shows the interface  $T$  and  $R$  ( $t$  and  $r$ ) of the FTO layer for forward (oFTOG) and for backward (GFTOo) light senses and the

air- $G$  or  $G$ -air interface  $T$  and  $R$  ( $t^G$  and  $r^G$ ). Figure 2(f) shows the absorptance determined at the FTO layer, from computed interface  $T$  and  $R$ , in both light senses ( $a^{oFTOG} = 1 - t^{oFTOG} - r^{oFTOG}$  and  $a^{GFTOo} = 1 - t^{GFTOo} - r^{GFTOo}$ ). At the LWRSS, when the FTO layer behaves as a film, the retrieved light absorption in the FTO layer is much lower from air to  $G$  light sense than from  $G$  to air light sense. At the SWRSS, where the FTO layer behaves as a substrate, similar absorption of the FTO layer is observed in both light senses. Note that between air and  $G$ ,  $t^G + r^G = 1$  since  $a_G = 0$ , as it is the case of a standard interface between two substrate mediums, where light can be only transmitted or reflected, but not extinct (absorbed or scattered). The  $\varepsilon$  for  $G$  and FTO layers are shown in Figure 2(g) and (h), respectively. Note that the 3eMR is observed in Figure 2(g) for the  $G$  layer in the solar spectrum and in Figure 2(h) for the FTO layer only at the SWRSS, i.e., where the FTO is considered as a substrate layer.

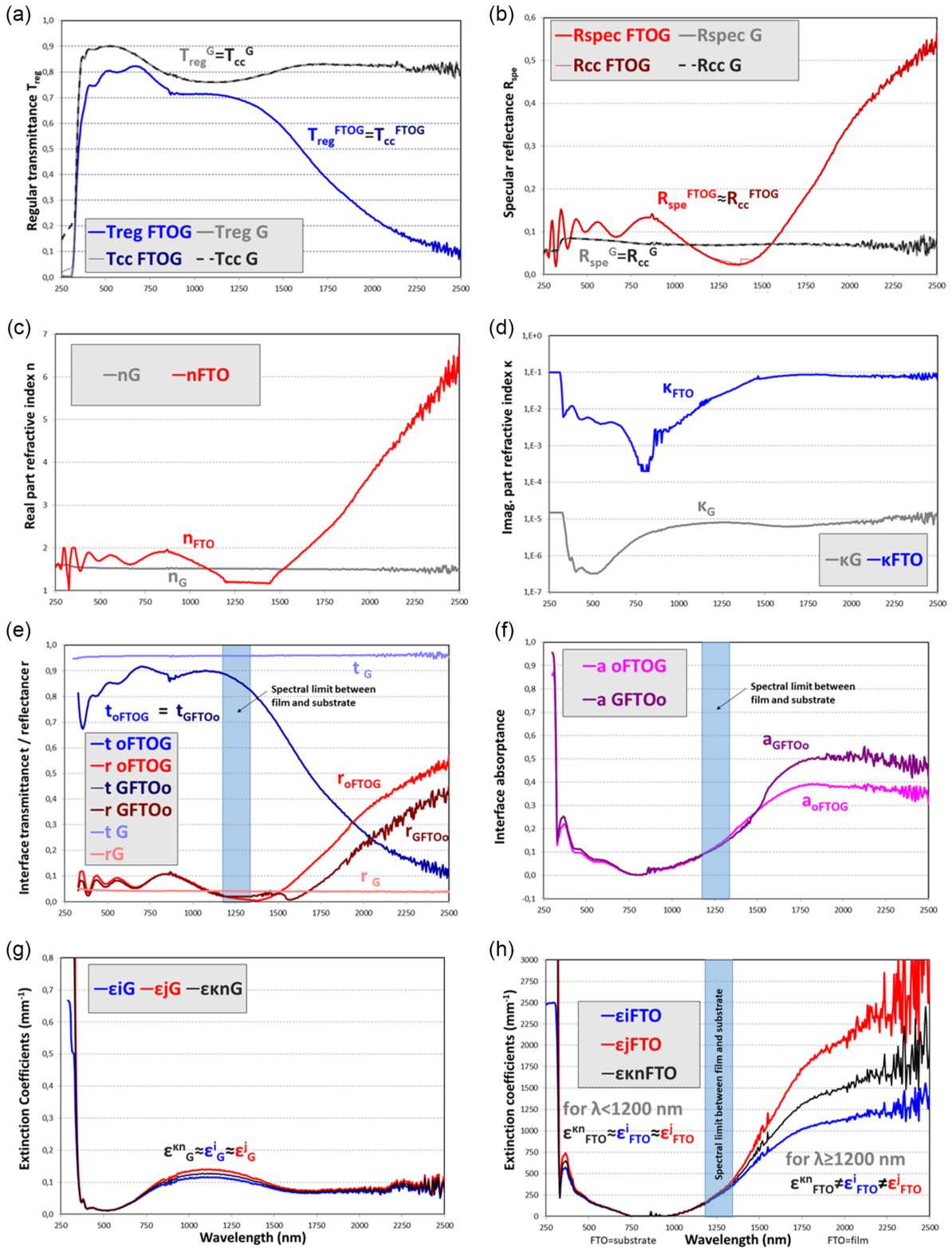
Figure 3 shows the  $\tau$  &  $\rho$  coefficients of the CEFs computed at  $z = \delta\delta$ , between air and FTO and at  $z = \delta$ , between FTO and  $G$ , for the LWRSS between 1200 nm to 2500 nm, where the FTO is considered as a film, and at  $z = 0$ , between  $G$  and air, for both SWRSS and LWRSS. Real parts ( $\tau'$  &  $\rho'$ ) of complex  $\tau$  and  $\rho$  obtained at air-FTO interface with  $z = \delta\delta$  in Figure 3(a), at FTOG interface with  $z = \delta$  in Figure 3(b) and at  $G$ -air interface with  $z = 0$  in Figure 3(c). Imaginary parts ( $\tau''$  &  $\rho''$ ) of the three interfaces are observed in Figure 3(d). Note that imaginary parts of  $G$ -air interface at  $z = 0$  are negligible values compared to air-FTO and FTOG interfaces, at  $z = \delta\delta$  and  $z = \delta$ , respectively. This is because  $\kappa^G$  is negligible compared to  $\kappa^{FTO}$ , in Figure 2(b). Figure 3(e) and (f) show real ( $\tau'$  &  $\rho'$ ) and imaginary ( $\tau''$  &  $\rho''$ ) parts of complex  $\tau$  and  $\rho$  coefficients, respectively. Figure 3(g) and (h) show WDD Bode magnitude and phase plots of CEF, respectively. Note that the same Bode phase plots ( $\theta_{\tau^{oFTOG}} = \theta_{\tau^{GFTOo}}$ ) are observed for outside air-FTOG and for  $G$ -FTO-outside air with  $\tau$  coefficients (as it was also observed in the ITOG sample [21]). Also in Figure 3(h), the same angle for Bode phase plots of  $\rho$  coefficients in  $\theta_{\rho^{GFTOo}}$  and  $\theta_{\rho^{oFTOG}}$  is observed at 1700 nm for the CEFs of the FTO layer considered as a film.

### 4.2. Light fluxes-thickness gradient plots at substrate layers of $G$ and FTOG samples

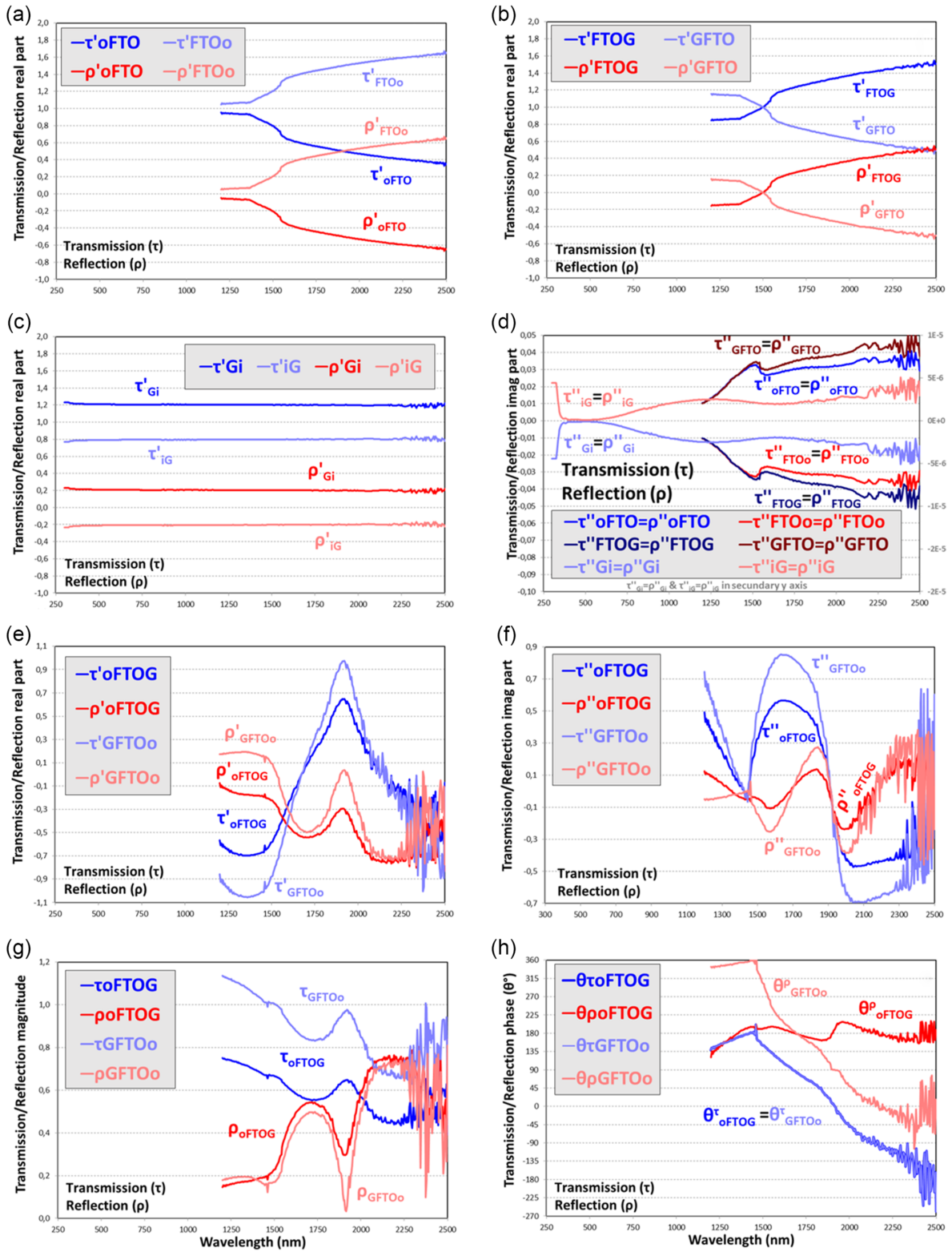
Collimated LF-TGP at the  $G$  substrate layers of  $G$  and FTOG samples are now determined by means of the procedure previously explained, i.e., from complex refractive index. For collimated LF-TG,  $(I^{\delta})^*$  and  $J^{\delta}$  have been interchanged with  $(I^Z)^*$  and  $J^Z$  at the 4FM-CDE in Equations (33) and (34), for determining the collimated for&back LF at each position inside of the  $G$  layer, obtaining Equations (53) and (54). Collimated LF-TGP of Figure 4 were obtained by computing five inner LF spectral values, at intermediate positions inside the substrate layer, in steps of 0.25 mm, for the  $G$  substrate layers of  $G$  and FTOG samples. Therefore, at the  $G$  substrate layer,  $z^0 = 0$ ,  $z^1 = 0.25$  mm,  $z^2 = 0.50$  mm,  $z^3 = 0.75$  mm,  $z^4 = 1.00$  mm,  $z^5 = 1.25$  mm, and being  $z^6 = 1.5$  mm =  $dz^G = \delta$ , i.e., the thickness of  $G$  substrate layers in both  $G$  and FTOG samples. Figure 4(a) and (b) show the for&back LF-TGP for the  $G$  sample. Figure 4(c) and (d) show the for&back LF-TGP for the FTOG sample. Collimated LF-TGP at the FTO layer of FTOG sample at the SWRSS, are now obtained from optical constants. For collimated LF-TGP,  $(I^{\delta\delta})^*$  and  $J^{\delta\delta}$  have been interchanged with  $(I^{ZZ})^*$  and  $J^{ZZ}$  in the 4FM-CDE in Equations (35) and (36), for determining collimated for&back LF at each place inside of the FTO layer, obtaining Equations (55) and (56). Figure 5 shows the LF-TGP at the FTO layer considered as a substrate, in the SWRSS, for for&back light senses.

Figure 2

(a) Transmittance and (b) reflectance measurements. Fitted optical constants: (c) real and (d) imaginary. (e) Interface transmittance and reflectance. (f) Optical absorptance. (g) Three-extinction matching requirement for G layer of the FTOG sample and (h) for FTO layer considered as film, for  $\lambda < 1200$  nm (spectral limit)



**Figure 3**  
 Real part of transmission and reflection coefficients for (a) air-FTO, (b) FTOG, and (c) G-air interfaces. (d) Imaginary parts. (e) Real part, (f) imaginary part, (g) magnitude, and (h) phase of the air-FTOG interface, for  $\lambda > 1200$  nm, considering the FTO layer as a film and not as a substrate



**Figure 4**  
**Collimated LF-TGP of the *G* substrate layer of the *G* sample and the FTOG sample. (a) Forward I and (b) backward J light fluxes of *G* sample. (c) Forward I and (d) backward J of FTOG sample**

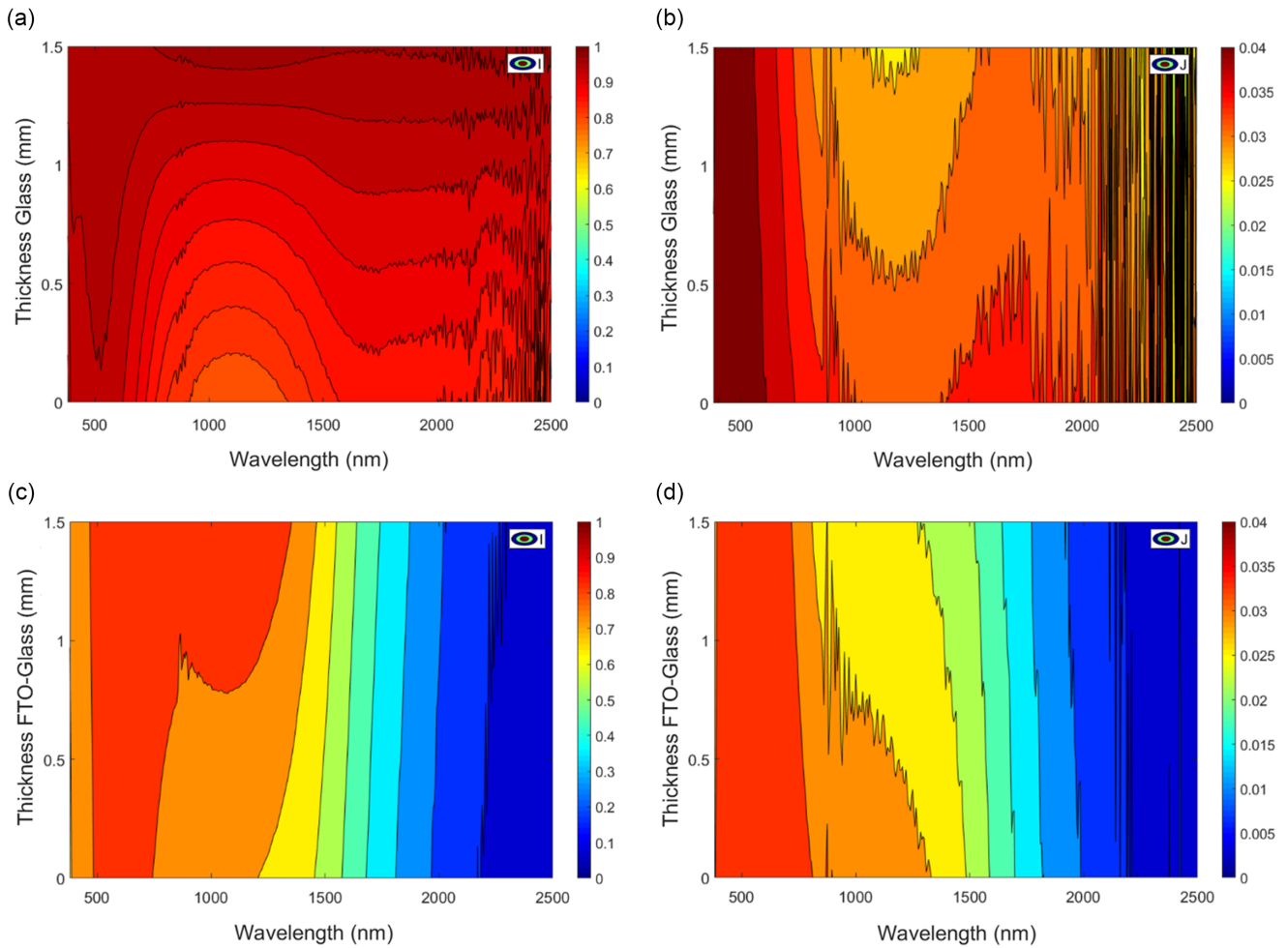
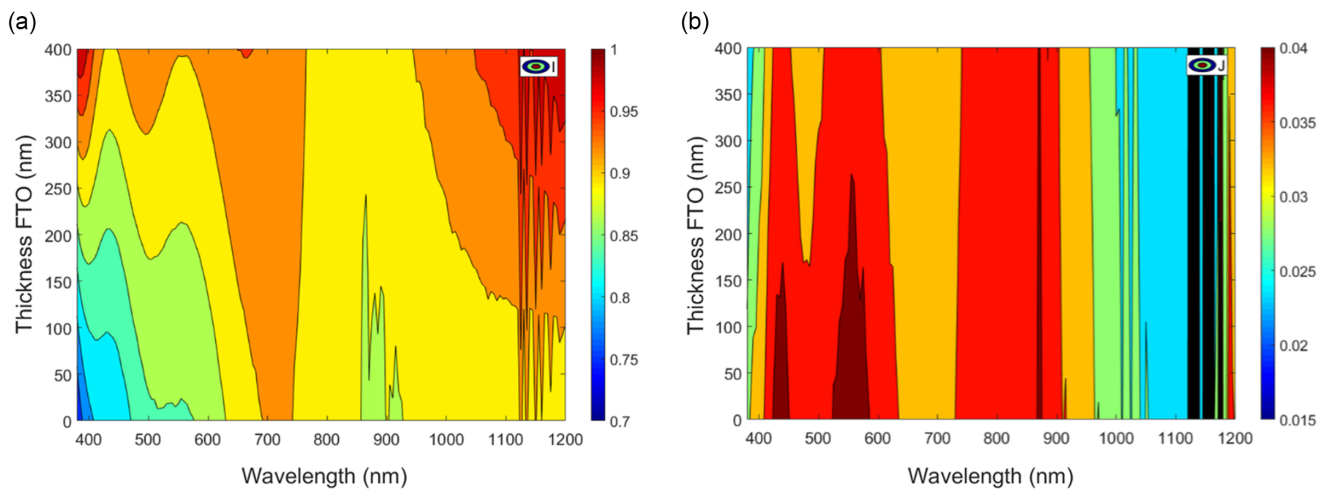


**Figure 5**  
**Collimated LF-TGP of the FTO layer of the FTOG sample for the SWRSS from 300 nm to 1200 nm, where the FTO layer is considered a substrate. (a) Forward I and (b) backward J**



$$(IZ)^* = \frac{I^0}{1 - \varepsilon_G^I \cdot Z} \quad (53)$$

$$J^Z = \frac{(J^0)^*}{1 + \varepsilon_G^I \cdot Z} \quad (54)$$

$$(IZZ)^* = \frac{I^\delta}{1 - \varepsilon_{FTO}^I \cdot Z} \quad (55)$$

$$J^{ZZ} = \frac{(J^\delta)^*}{1 + \varepsilon_{FTO}^I \cdot Z} \quad (56)$$

### 4.3. Complex electric fields-thickness gradient plots at FTO layer of FTOG sample considered film

$F^\delta$  is computed using Equation (57), as it was carried out for the ITOG sample in Barrios [21]. In this case, for the FTOG sample,  $F^\delta$  is shown in Figure 6. Equations (51) and (52) were required for Re&Im-P of intermediate CEFs determined with 80 nm steps. CEF-TGP are here determined by means of Equation (58) at four intermediate positions (i.e.,  $dz_{FTO}^1 = 80$  nm,  $dz_{FTO}^2 = 160$  nm,  $dz_{FTO}^3 = 240$  nm and  $dz_{FTO}^4 = 320$  nm, being  $dz_{FTO}^0 = 0$  nm and  $dz_{FTO}^5 = 400$  nm) inside the FTO layer considered as film at the LWRSS. Following Equations (51) and (52), Equation (15) is Euler like expression  $e^{ix} \cdot e^{iy}$ ,  $e^y \cdot e^{ix} = e^y \cdot [\cos(x) + i \cdot \sin(x)]$ , being  $x = -2\pi n^{FTO} d / \lambda^{FTO} = 2\pi n^{FTO} d \cdot n^{FTO} / \lambda$  and  $y = 2\pi \kappa^{FTO} d / \lambda^{FTO} = 2\pi \kappa^{FTO} d \cdot n^{FTO} / \lambda$  in Equation (58).

$$F^\delta = \frac{\tau_{oFTOG} \cdot \rho_{Gi} \cdot (\Delta_f(dz^G))^2}{1 - \rho_{GFTOo} \cdot \rho_{Gi} \cdot (\Delta_f(dz^G))^2} \quad (57)$$

$$\Delta_f(d) = \frac{E_2}{E_1} = \exp\left(-\frac{2\pi \kappa^{FTO} d}{\lambda} n^{FTO}\right) \cdot \left\{ \cos\left(-\frac{2\pi n^{FTO} d}{\lambda} n^{FTO}\right) + i \cdot \sin\left(-\frac{2\pi n^{FTO} d}{\lambda} n^{FTO}\right) \right\} \quad (58)$$

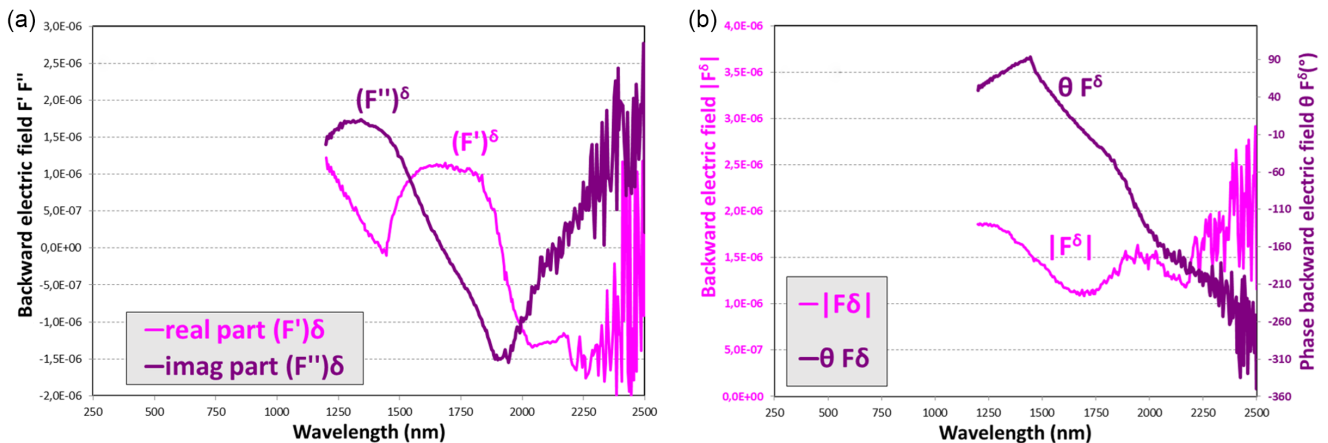
Then, using Equation (16) and substituting the positions (1) and (2) with the values of the CEFs E and F at the interfaces of the

FTO layer (at  $z = \delta\delta$  and at  $z = \delta$ ), Equation (59) was applied at the four intermediate positions between the extremes or interfaces, using the  $\Delta_f(d)$  film attenuations obtained with Equation (58). Hence, the film layer matrix  $N_{EF}^{FTO}$  of Equation (59) is computed at the four intermediate positions in order to obtain the values of the intermediate CEFs  $E$  and  $F$ . Then, Figure 7 shows the forward  $E$  and backward  $F$  real (a and b) and imaginary (c and d) parts of CEF, and the WDD Bode magnitude (e and f) and phase (g and h). Despite the apparently disordered spectral values observed for Re&Im-P, and also for the phase plots, the magnitude plots show an order of the CEF  $E$  and  $F$ , with higher values obtained near the top interface at  $z = \delta\delta$ , and lower values obtained near the middle interface at  $z = \delta$ , in Figure 1(d). Figure 8 uses the plots of Figure 7 to obtain the CEF-TGP, for Re&Im-P and for Bode magnitude and phase WDD.

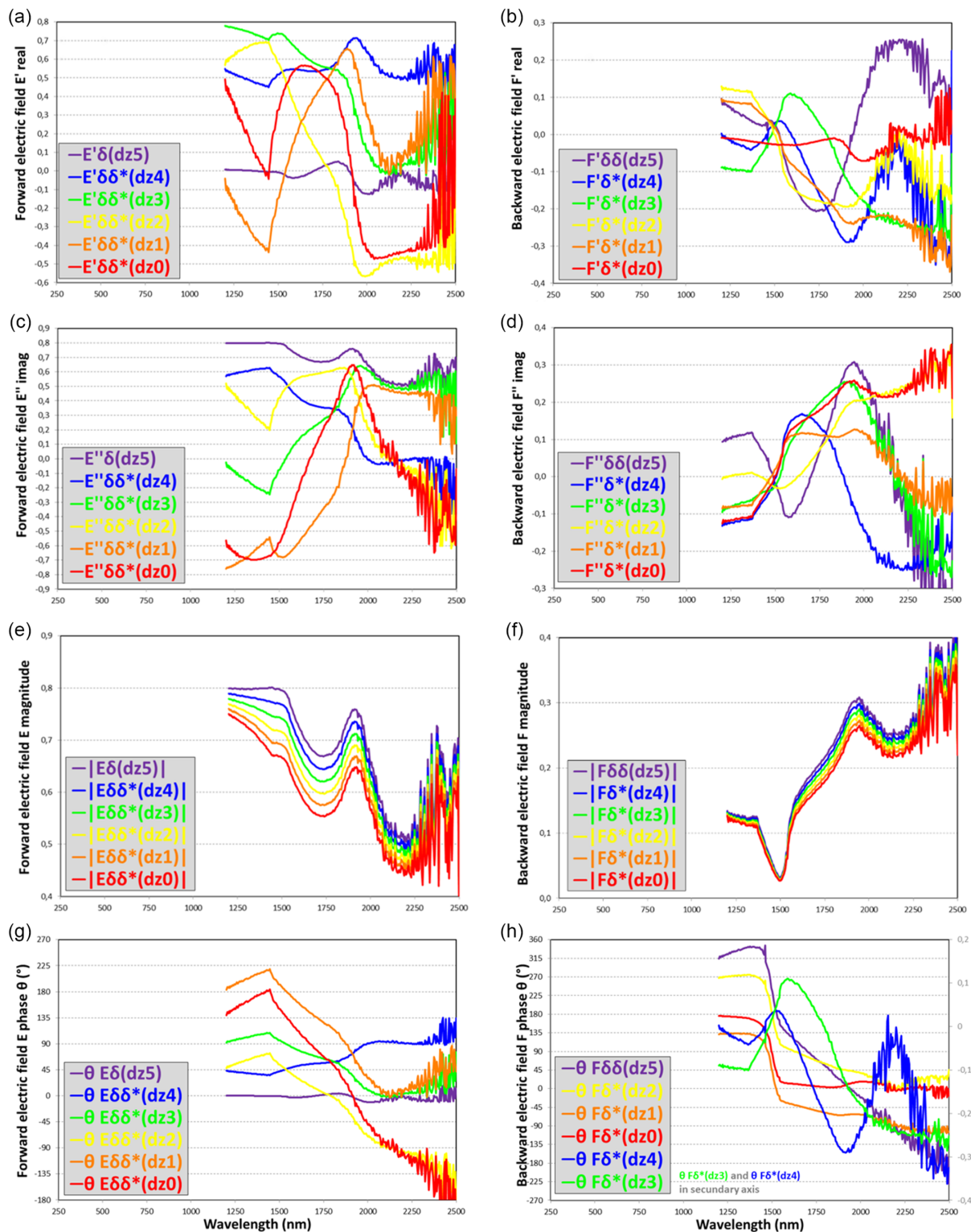
$$\begin{bmatrix} (E^{\delta\delta})^* \\ F^{\delta\delta} \end{bmatrix} = \begin{bmatrix} \frac{1}{\Delta_f(d)} & 0 \\ 0 & \Delta_f(d) \end{bmatrix} \cdot \begin{bmatrix} (E^\delta) \\ (F^\delta)^* \end{bmatrix} = N_{EF}^{FTO}(d) \cdot \begin{bmatrix} (E^\delta) \\ (F^\delta)^* \end{bmatrix} \quad (59)$$

Figure 9 shows the Nyquist WDD in the LWRSS, from up to down (violet to red colors) for  $E$  and from down to up (red to violet colors) for  $F$ . Figure 9(a) and (b) shows a 3D plot of imaginary versus real parts of the CEFs  $E$  and  $F$ , respectively (check Figure 1(d) with  $F^\delta \approx 0$ ). For a better visualization, Figure 9(c) and (d) shows the wall projections of the Nyquist WDD plots of Figure 9(a) and (b). In order to observe the sense of increment of wavelength, the maximum considered wavelength  $\lambda_{max}$  is indicated and placed besides the corresponding plot at the inside of Figure 9(e) and (f) of the Nyquist WDD for CEF  $E$  and  $F$  respectively. Here  $\lambda_{max} = 2250$  nm, instead of 2500 nm, in order to avoid noise in the plots due to the high oscillations in this range of wavelength, observed in Figures 7 and 8. Note that in Figure 9(e) and (f), the minimum wavelength of the LWRSS, i.e.,  $\lambda_{min} = 1200$  nm, that is the spectral limit of the optical behavior between a substrate and a film, was not indicated.

**Figure 6**  
CEP  $F^\delta$  in backward sense reaching the FTO bottom interface at  $z = \delta$  determined using Equation (57). (a) Re&Im-P ( $F'$ ) $^\delta$  and ( $F''$ ) $^\delta$ . (b) Magnitude  $|F^\delta|$  and  $\theta$  phase ( $^\circ$ ) of  $F^\delta$



**Figure 7**  
 Collimated CEFs (forward E and backward J) of the FTO layer of the FTOG sample for the LWRSS, from 1200 nm to 2500 nm, where the FTO layer is considered as a film. Real parts: (a) E and (b) F. Imaginary parts: (c) E and (d) F. Magnitude: (e) E and (f) F. Phases: (g) E and (h) F



**Figure 8**  
**Collimated CEF-TGPs (forward E and backward F) of the FTO layer of the FTOG sample for the LWRSS, from 1200 nm to 2500 nm, where the FTO layer is considered a film. Real parts: (a) E and (b) F. Imaginary parts: (c) E and (d) F. Magnitudes: (e) E and (f) F. Phases: (g) E and (h) F**

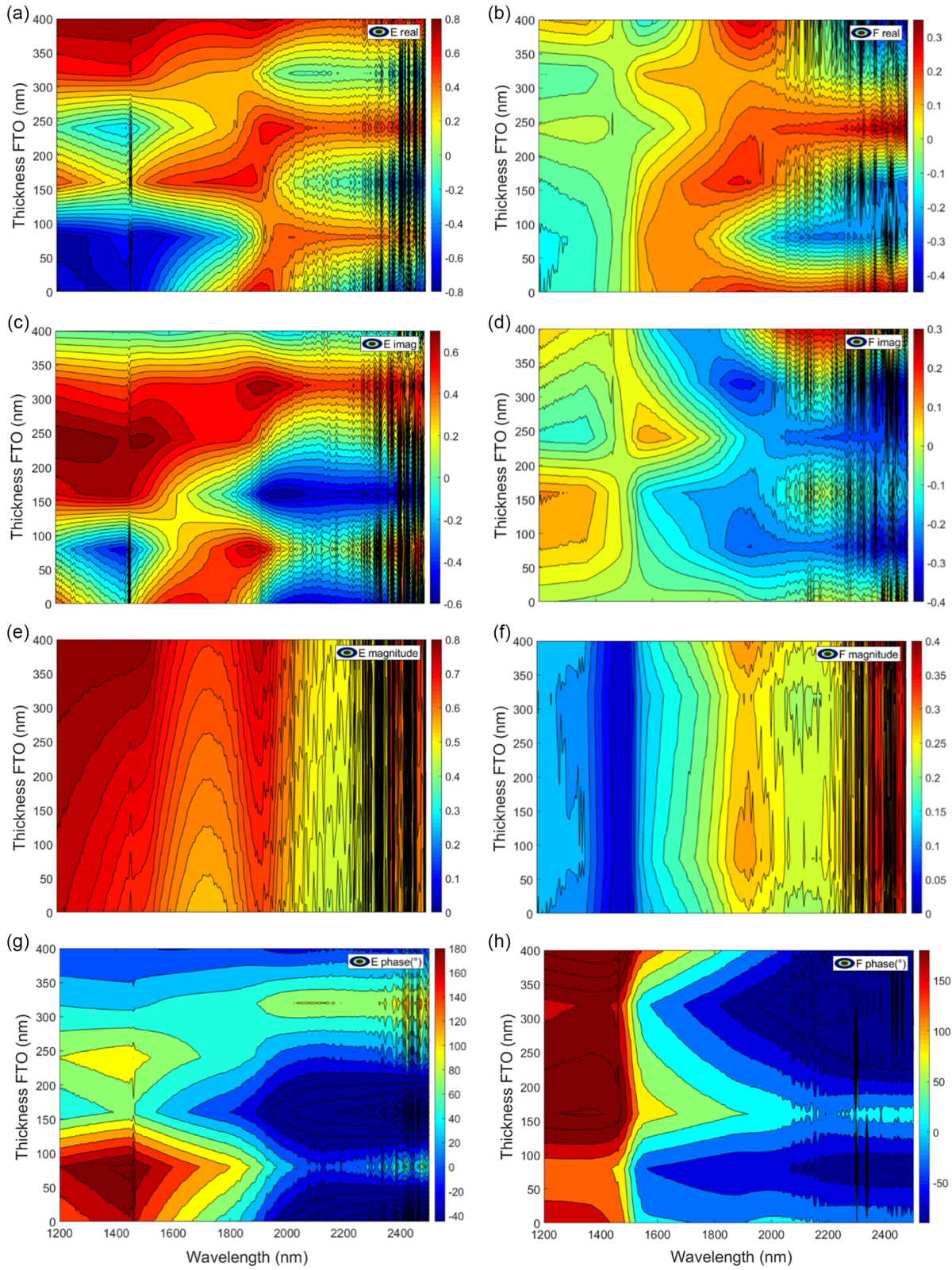
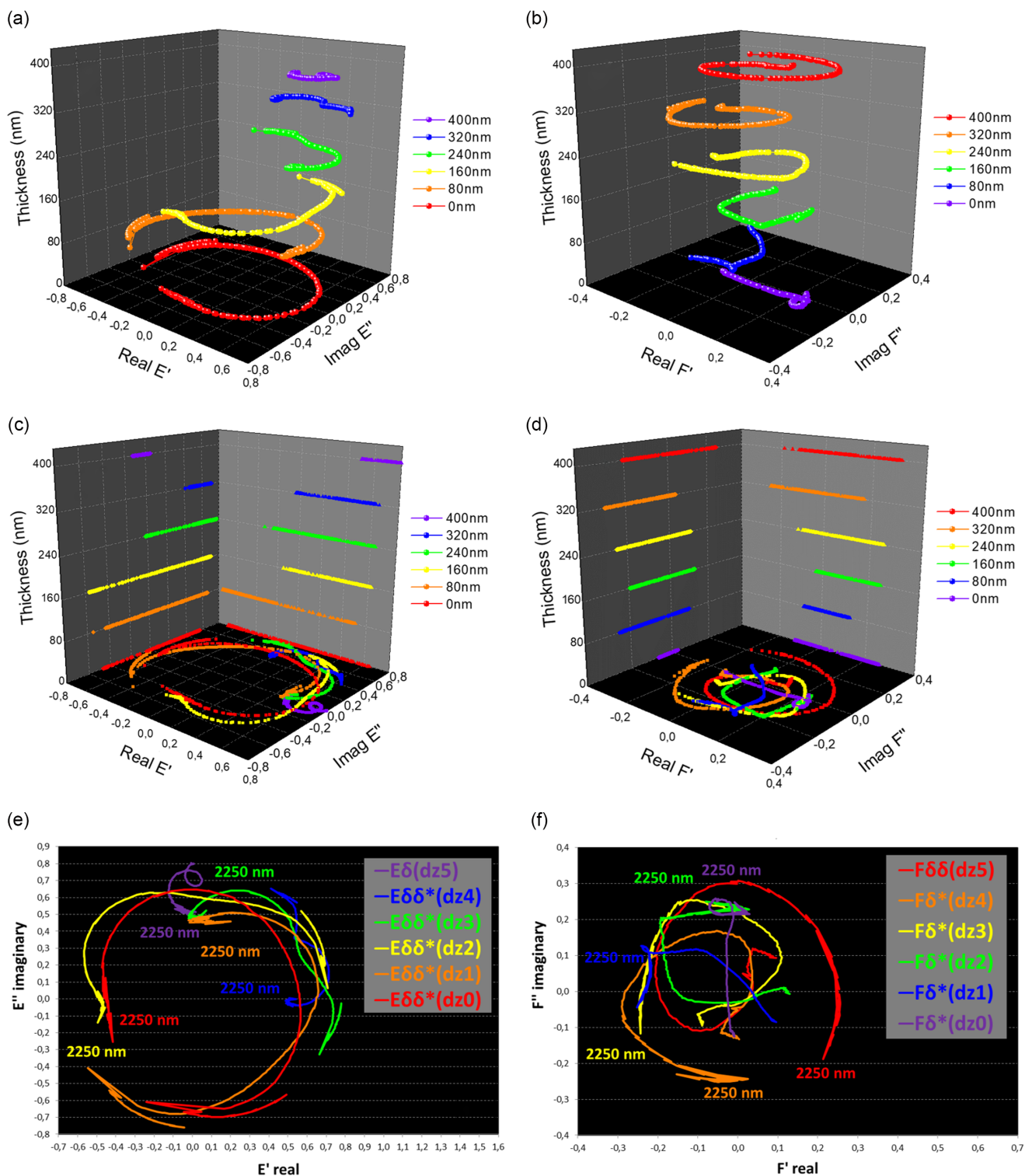


**Figure 9**  
**Imaginary parts versus real parts or Nyquist WDD plots for (a) (c) (e) forward E and for (b) (d) (f) backward F. CEF inside the FTO layer considered as a film, from 1200 nm to 2500 nm**



## 5. Conclusion

The complex refractive index of a TC FTO layer has been obtained and used to obtain the TGP of collimated for&back LF in the  $G$  substrate of the FTOG sample (FTO layer placed over a  $G$  substrate) together with the  $G$  sample (a single  $G$  substrate layer). For the  $G$  sample and for the FTOG sample, accurate values of collimated LFs were demonstrated thanks to the  $3\epsilon$ MR, a phenomenon observed when the same  $\epsilon$  is obtained by means of three different ways, i.e., from the complex refractive index and from the LF of the 4FM-CDE. The  $3\epsilon$ MR was also used in this work to determine the spectral limit of the optical behavior as a film and as a substrate, of the FTO layer, observed at 1200 nm. FTO layer behaves as a substrate for the SWRSS, from 250 nm to 1200 nm, and behaves as a film for the LWRSS, from 1200 nm to 2500 nm. Soft transition and continuity of results in the spectral limit validate it. Compared to ITO 26 nm, the spectral limit behavior would be expected at 73 nm, which is outside of the WRSS used in the  $T$  and  $R$  measurements. The  $\epsilon$  coefficients computed from the complex refractive index were obtained considering that the wavelength of light is compressed ( $\lambda_n = \lambda/n$ ) when it travels inside of a medium different from free space or air, such as at  $G$  and at FTO substrate layers. Note that the decrement of speed of light is caused by a decrement of the wavelength and not by a decrement of the frequency. Thanks to the  $3\epsilon$ MR phenomenon observed at the  $G$  layer of the  $G$  and FTOG samples in the WRSS and at FTO layer for the SWRSS, behaving as a substrate, the FTO layer of 400 nm is considered a film for LWRSS, i.e., for wavelength higher than 1200 nm, that is three times the thickness. Nyquist WDD (imaginary versus real parts) and Bode WDD (spectral magnitude and phase) of CEFs  $E$  and  $F$  were determined at four different positions inside the FTO layer, besides the obtained at top and middle interfaces. From them, TGP at the FTO layer considered as a film, at the LWRSS, were determined and plotted. Then, Nyquist WDD of for&back  $E$  and  $F$  CEFs of light at the FTO layer considered as a film were determined. In original Nyquist diagrams (depending on frequency of complex electrical impedance, instead of on wavelength of CEFs), the semicircular behavior is associated with the electrical capacitor, placed in parallel to a resistance, and this shunt in series with another resistance (Randles cell) [30]. For the CEF related to the light inside the FTOG sample, the cause of the semicircular behavior should be an optical  $\epsilon$  effect observed for the forward CEF  $E$  in Figure 9(e), at the top outer interface with  $z = \delta\delta$ , and for the backward CEF  $F$ , in Figure 9(f), at the top inner interface with  $z = \delta$ .

The complex refractive index of FTO determined in this document and the complex refractive index of the electrolyte layer determined in a previous work [20] are thought to be used by the author in a new next research, for computing the complex refractive index of the inner active layers for multilayer  $\text{WO}_3$ -NiO-based ECD samples. Searching to obtain the  $3\epsilon$ MR, the study would verify if the spectral limit of the optical behavior for the  $\text{WO}_3$  and NiO layers of 120 nm and 240 nm thicknesses would take place at wavelengths three times the thicknesses, as it was observed in this work at 1200 nm for the FTO layer of 400 nm thickness. For ECD11 (120 nm thicknesses for both  $\text{WO}_3$  and NiO), dividing the SWRSS into two ranges: From 250 nm to 360 nm, both FTO- $\text{WO}_3$  and FTO-NiO interfaces between two substrate layers. From 360 nm to 1200 nm, both FTO- $\text{WO}_3$  and FTO-NiO interfaces between a substrate layer (FTO) and a film layer ( $\text{WO}_3$  and NiO). For ECD12 (120 nm thickness for  $\text{WO}_3$  and 240 nm thickness NiO), dividing the SWRSS into three ranges: From 250 nm to 360 nm, FTO- $\text{WO}_3$  interface between two substrate layers. From 360 nm to 720 nm, FTO-NiO interface

between two substrate layers. From 720 nm to 1200 nm, both FTO- $\text{WO}_3$  and FTO-NiO interfaces between a substrate (FTO) and a film layer ( $\text{WO}_3$  and NiO). For ECD21 (240 nm thickness for  $\text{WO}_3$  and 120 nm thickness NiO), dividing the SWRSS into three ranges: From 250 nm to 360 nm, FTO-NiO interface between two substrate layers. From 360 nm to 720 nm, FTO- $\text{WO}_3$  interface between two substrate layers. From 720 nm to 1200 nm, both FTO- $\text{WO}_3$  and FTO-NiO interfaces between a substrate (FTO) and a film layer ( $\text{WO}_3$  and NiO). For ECD22 (240 nm thicknesses for both  $\text{WO}_3$  and NiO), dividing the SWRSS into two ranges: From 250 nm to 720 nm, both FTO- $\text{WO}_3$  and FTO-NiO interfaces between two substrate layers. From 720 nm to 1200 nm, both FTO- $\text{WO}_3$  and FTO-NiO interfaces between a substrate layer (FTO) and a film layer ( $\text{WO}_3$  and NiO).

Finally and as future works, using the expected optical constants of separated active layers ( $\text{WO}_3$  and NiO) of ECDs, it would be interesting to obtain their Nyquist WDD. The observation of the  $3\epsilon$ MR phenomenon including layers at the sandwich structure behaving as substrate and as film, for different WRSS, would lead to the determination of intrinsic (4FM) and extrinsic (2FM) scattering and absorption coefficients of each active layer ( $\text{WO}_3$  and NiO) in ECDs, for both bleached-off and colored-on optical states.

## Recommendations

The reader is suggested to read a similar study using a thin film of ITO layer over a glass substrate, in reference [21].

## Acknowledgements

The author is grateful to Laboratory for Spectroscopy of Materials of the National Institute of Chemistry of Ljubljana, for providing the  $G$  and FTOG samples and the used spectrometer required for measurements, to Grupo de Displays y Aplicaciones Fotónicas, Dept. Tecnología Electrónica, and to the mobility grants of Universidad Carlos III de Madrid. for supporting research in Slovenia.

## Ethical Statement

This study does not contain any studies with human or animal subjects performed by the author.

## Conflicts of Interest

The author declares that he has no conflicts of interest to this work.

## Data Availability Statement

Data sharing is not applicable to this article as no new data were created or analyzed in this study.

## Author Contribution Statement

**David Barrios-Puerto:** Conceptualization, Methodology, Software, Validation, Formal analysis, Investigation, Resources, Data curation, Writing – original draft, Writing – review & editing, Visualization, Supervision, Project administration.

## References

- [1] Granqvist, C. G. (2007). Transparent conductors as solar energy materials: A panoramic review. *Solar Energy*

- Materials and Solar Cells*, 91(17), 1529–1598. <https://doi.org/10.1016/j.solmat.2007.04.031>
- [2] Ramírez-Amador, R., Alvarado-Pulido, J. J., Martínez-Hernández, H. P., Cortes-Maldonado, R., Alcántara-Iniesta, S., Flores-Carrasco, G., . . . , & López-Salazar, P. (2023). Study of fluorine-doped tin oxide thin films deposited by pneumatic spray pyrolysis and ultrasonic spray pyrolysis: A direct comparison. *Materials Research Express*, 10(6), 066402. <https://doi.org/10.1088/2053-1591/acda1a>
- [3] Thomas, R., Mathavan, T., Ganesh, V., Yahia, I. S., Zahran, H. Y., AlFiafy, S., & Kathalingam, A. (2020). Investigation of erbium co-doping on fluorine doped tin oxide via nebulizer spray pyrolysis for optoelectronic applications. *Optical and Quantum Electronics*, 52(5), 248. <https://doi.org/10.1007/s11082-020-02376-8>
- [4] Toral-López, A., Pérez, M. M., Rodríguez-Águila, A. B., Cardona, J. C., Ionescu, A. M., & Godoy, A. (2023). Investigation of the optical properties of indium tin oxide thin films by double integration sphere combined with the numerical IAD method. *Materials*, 16(4), 1425. <https://doi.org/10.3390/ma16041425>
- [5] Křepelka, J. (2023). Exact solution of maximally flat antireflection coatings for coherent and incoherent light. *arXiv Preprint: 2308.02516*.
- [6] Shklyae, A. A., Utkin, D. E., Zheng, Z., & Tsarev, A. V. (2023). Redirecting incident light with Mie resonance-based coatings. *Photonics*, 10(11), 1286. <https://doi.org/10.3390/photonics10111286>
- [7] Ballester, M., Marquez, E., Bass, J., Wuersch, C., Willomitzer, F., & Katsaggelos, A. K. (2024). Review and novel formulae for transmittance and reflectance of wedged thin films on absorbing substrates. *arXiv Preprint: 2409.02323*.
- [8] Stenzel, O., & Wilbrandt, S. (2025). Theoretical aspects of thin film optical spectra: Underlying models, model restrictions and inadequacies, algorithms, and challenges. *Applied Sciences*, 15(4), 2187. <https://doi.org/10.3390/app15042187>
- [9] Sergienko, A. A., Pushkin, D. B., Konotopov, P. A., & Cheremnykh, A. D. (2023). Opredeleniye pokazateley prelomleniya materialov pri modelirovani mnogosloynnykh zerkal [Determination of refractive indices of materials in modeling multilayer mirrors]. *Industrial Laboratory. Diagnostics of Materials*, 89(5), 36–40. <https://doi.org/10.26896/1028-6861-2023-89-5-36-40>
- [10] Dvořák, J., Vohánka, J., Buršíková, V., Franta, D., & Ohlídal, I. (2023). Optical characterization of inhomogeneous thin films deposited onto non-absorbing substrates. *Coatings* 13(5), 873–889. <https://doi.org/10.3390/coatings13050873>
- [11] Nosidlak, N., Jaglarz, J., Vallati, A., Dulian, P., Jurzecka-Szymacha, M., Gieraltowska, S., . . . , & Godlewski, M. (2023). The optical properties of thin film alloys of ZnO, TiO<sub>2</sub> and ZrO<sub>2</sub> with Al<sub>2</sub>O<sub>3</sub> synthesised using atomic layer deposition. *Coatings*, 13(11), 1872. <https://doi.org/10.3390/coatings13111872>
- [12] Egorov, N. V., Fedorov, A. G., & Trofimov, V. V. (2024). Metody matrity perenosa i rasseyaniya dlya chislennogo opredeleniya koeffitsiyentov otrazheniya i prelomleniya tonkoplenochnykh materialov [Comparison transfer matrix methods and scattering matrix method for investigation the optical properties of multilayer structures]. *Vestnik of Saint Petersburg University. Applied Mathematics. Computer Science. Control Processes*, 20(4), 432–445. <https://doi.org/10.21638/spbu10.2024.401>
- [13] Adnan, M., Jamil, M., Ramzan, B., Hussain, T., Afaq, A., & Ghani, M. (2024). Determination of the optical properties of tungsten trioxide thin film using the transfer matrix method. *Indian Journal of Physics*, 99(5), 1645–1649. <https://doi.org/10.1007/s12648-024-03401-2>
- [14] Ren, Y., Kong, D., Tan, W., Wang, J., Chen, T., Zhang, Q., & Xia, W. (2024). Simultaneous determination of the scattering and absorption coefficients of turbid media based on Mueller matrix. *Journal of Modern Optics* 71(10–12), 354–363. <https://doi.org/10.1080/09500340.2024.2422905>
- [15] Isoe, W. M., Mageto, M. J., Maghanga, C. M., Mwamburi, M. M., & Odari, B. V. (2023). Optical modelling of TCO based FTO/TiO<sub>2</sub> multilayer thin films and simulation in hydrogenated amorphous silicon solar cell. *Scientific African*, 20, e01678. <https://doi.org/10.1016/j.sciaf.2023.e01678>
- [16] Born, M., & Wolf, E. (1970). *Principles of optics: Electromagnetic theory of propagation, interference and diffraction of light* (4th Rev. ed.). UK: Pergamon Press. <https://doi.org/10.1017/CBO9781139644181>
- [17] Knittel, Z. (1976). *Optics of thin films: An optical multilayer theory*. UK: Wiley.
- [18] Harbecke, B. (1986). Coherent and incoherent reflection and transmission of multilayer structures. *Applied Physics B Photophysics and Laser Chemistry*, 39(3), 165–170. <https://doi.org/10.1007/BF00697414>
- [19] Pfrommer, P., Lomas, K. J., Seale, C., & Kupke, C. (1995). The radiation transfer through coated and tinted glazing. *Solar Energy*, 54(5), 287–299. [https://doi.org/10.1016/0038-092X\(94\)00132-W](https://doi.org/10.1016/0038-092X(94)00132-W)
- [20] Puerto, D. B. (2024). Intrinsic and extrinsic scattering and absorption coefficients new equations in four-flux and two-flux models used for determining light intensity gradients. *Journal of Optics and Photonics Research*, 1(3), 131–144. <https://doi.org/10.47852/bonviewJOPR42022261>
- [21] Barrios, D. (2024). Optical constants and thickness gradients for light intensities in glass substrate layers and for complex electric fields in indium tin oxide (ITO) transparent conductor thin film layer, using Bode and Nyquist wavelength-dependent diagrams. *Journal of Physics: Conference Series*, 2796(1), 012019. <https://doi.org/10.1088/1742-6596/2796/1/012019>
- [22] Barrios, D. (2025). New procedure for intrinsic scattering and absorption coefficients of four-flux model for suspended particle device and polymer dispersed liquid crystal. *Optics Communications*, 582, 131594. <https://doi.org/10.1016/j.optcom.2025.131594>
- [23] Niklasson, G. A., & Granqvist, C. G. (2007). Electrochromics for smart windows: Thin films of tungsten oxide and nickel oxide, and devices based on these. *Journal of Materials Chemistry*, 17(2), 127–156. <https://doi.org/10.1039/B612174H>
- [24] Beasley, K., Atkins, J. T., & Billmeyer F. W. (1967). Scattering and absorption of light in turbid media. In *2nd Interdisciplinary Conference on Electromagnetic Scattering*, 765–784.
- [25] Carter, E. C. (2023). Billmeyer, Fred Wallace, Jr. In R. Shamey (Ed.), *Encyclopedia of color science and technology* (pp. 101–103). Springer. [https://doi.org/10.1007/978-3-030-89862-5\\_337](https://doi.org/10.1007/978-3-030-89862-5_337)
- [26] Maheu, B., Letoulouzan, J. N., & Gouesbet, G. (1984). Four-flux models to solve the scattering transfer equation in terms

- of Lorenz-Mie parameters. *Applied Optics*, 23(19), 3353. <https://doi.org/10.1364/AO.23.003353>
- [27] Kubelka, P. (1948). New contributions to the optics of intensely light-scattering materials. Part I. *Journal of the Optical Society of America*, 38(5), 448–457. <https://doi.org/10.1364/JOSA.38.000448>
- [28] Levinson, R., Berdahl, P., & Akbari, H. (2005). Solar spectral optical properties of pigments– Part I: model for deriving scattering and absorption coefficients from transmittance and reflectance measurements. *Solar Energy Materials and Solar Cells*, 89(4), 319–349. <https://doi.org/10.1016/j.solmat.2004.11.012>
- [29] Bohren, C. F. & Huffman, D. R. (1983). *Absorption and scattering of light by small particles*. USA: Wiley. <https://doi.org/10.1002/9783527618156>
- [30] Barsoukov, E., & Macdonald, J. R. (2005). *Impedance spectroscopy: Theory, experiment, and applications* (2nd ed.). USA: Wiley. <https://doi.org/10.1002/0471716243>

**How to Cite:** Barrios-Puerto, D. (2025). Spectral Limit of the Optical Behavior Between Film and Substrate for a Fluorine-Doped Tin Oxide (FTO) Transparent Conductive Layer. *Journal of Optics and Photonics Research*. <https://doi.org/10.47852/bonviewJOPR52025408>

## Appendix

### Nomenclature

#### Greek symbols

$\alpha$	intrinsic scattering coefficient
$\beta$	intrinsic absorption coefficient
$\delta$	$z$ coordinate at top inner interface
$\delta\delta$	$z$ coordinate at top outer interface
$\Delta_f(d)$	film layer attenuation
$\Delta_s(d)$	substrate layer attenuation
$\varepsilon$	extinction coefficient
$\varepsilon^{kn}$	$\varepsilon$ obtained from optical constants
$\varepsilon_i$	$\varepsilon$ obtained from forward CDE
$\varepsilon_j$	$\varepsilon$ obtained from backward CDE
$\kappa$	imaginary part of complex refractive index
$\lambda$	wavelength
$\tau$	Fresnel transmission coefficient
$\tau^S$	$\tau$ for S polarization
$\tau^P$	$\tau$ for P polarization
$\rho$	Fresnel reflection coefficient
$\rho^S$	$\rho$ for S polarization
$\rho^P$	$\rho$ for P polarization

#### English Symbols

0	$z$ coordinate at bottom interface
2FM	two-flux model
3eMR	three-extinction matching requirement
4FM	four-flux model
ACP	average crossing parameter
cc	collimated-collimated
cd	collimated-diffuse
CEF	complex electric fields
CDE	collimated differential equations
dz	thickness of a layer
DDE	diffuse differential equations
E	forward electric field
ECD	electrochromic device
F	backward electric field
for&back	forward and backward
FTO	fluorine-doped indium oxide
FTOG	bilayer FTO-glass sample

FSR	forward scattering ratio
$G$	glass
GEG	glass/electrolyte/glass
$i$	forward light sense
$I$	collimated forward light flux
$I^0$	$I$ at bottom interface
$I^\delta$	$I$ at top inner interface
$I^{\delta\delta}$	$I$ at top outer interface
ITO	tin-doped indium oxide
ITOG	bilayer ITO-glass sample
$j$	backward light sense
$J$	collimated backward light flux
$J^0$	$J$ at bottom interface
$J^\delta$	$J$ at top inner interface
$J^{\delta\delta}$	$J$ at top outer interface
$K$	extrinsic absorption coefficient
LF	light flux
LWRSS	longer wavelength range of the solar spectrum
$M_{oi}$	interface matrix between medium outside “o” and inside “i” mediums
$N_s$	substrate “s” layer matrix
$n$	real part of complex refractive index
$n'$	complex refractive index
PDLC	polymer-dispersed liquid crystal
$R$	reflectance
$r$	collimated interface reflectance
$r_{oFTOG}$	collimated reflectance of FTO from outside air to glass
$r_{GFTOo}$	collimated reflectance of FTO from glass to outside air
$R_{cc}$	calculated specular reflectance
$R_{spe}$	measured specular reflectance
Re&Im-P	real and imaginary parts
$S$	extrinsic backscattering coefficient
SPD	suspended particle device
SWRSS	shorter wavelength range of the solar spectrum
$T$	transmittance
$t$	collimated interface transmittance
TGP	thickness gradient plots
$t_{oFTOG}$	collimated transmittance of FTO from outside air to glass
$t_{GFTOo}$	collimated transmittance of FTO from glass to outside air
$T_{cc}$	calculated regular transmittance
$T_{reg}$	measured regular transmittance
TSLSS	three substrate layers sandwich structure
WRSS	wavelength range of the solar spectrum
WDD	wavelength-dependent diagrams